An Implicit Simulation Framework for Well Acidizing Process in Carbonate Reservoirs

Thesis submitted to the
Delft University of technology (TU Delft)
in partial fulfillment of the requirements for the degree

MASTER OF SCIENCE
IN
APPLIED EARTH SCIENCES
(PETROLEUM ENGINEERING AND GEOSCIENCES)

By

JULES CLARKE

The work has been conducted as a collaboration project between Delft Advanced Reservoir Simulation (DARSim) group and AkzoNobel Co.

Principle Advisor: Dr. H. Hajibeygi, TU Delft
Co-Advisor: Dr. A. Ameri, Akzonobel Co.
Daily supervisor: Ir. M. Cusini, TU Delft

Other committee members (all TU Delft faculty):
Prof.dr.ir. M. Bakker; Prof.dr. W. Rossen; Dr. D. Voskov

28 JULY 2017

Abstract

This thesis elaborates on a newly developed Fully Implicit (FIM) simulation model that captures the full coupling of reaction kinetics and fluid dynamics during carbonate matrix acidizing at an extensive (near wellbore) scale. The framework describes the physical processes at reservoir scale, by accounting for upscaled pore-scale-based quantities for reaction rates and reservoir flow properties (e.g. permeability and porosity). The coupled Darcy-Stokes system of equation, as represented in a unified Brinkman formulation, is incorporated in the model to account for free flow (wormholes) and flow trough porous media. The model is built to investigate the subsurface behavior of the specific (Dissolvine® Stimwell) acid developed by AkzoNobel Co. Dissolvine Stimwell includes chelating agents which have, under specific conditions, significant advantages over conventional acids. Generally, carbonate acidizing treatment experiments are conducted at the core scale. However, in Salt Lake City in Utah a carbonate acidizing experiment was carried out at unprecedented (above core) scale. The corresponding results are compared with the developed model to validate the dependency of the wormhole formation with the injection rate. In addition, the reduction in the skin factor is briefly addressed. Apart from the FIM simulation development for coupled reactive transport equation with Brinkman flow formula, the other valuable contribution of this work lies on the validation with experimental results at the unprecedented scale.

TABLE OF CONTENTS

List of Tables

List of Figures

Figure **Page**

CHAPTER 1

INTRODUCTION

Near wellbore[1] damage is generally inflicted during the completion or drilling phase of the field development cycle. During these phases, a pressure differential causes fines to migrate in or out of the formation. It is likely that these fines get trapped in the near wellbore formation. These fines get trapped in the pores, near wellbore, which results in a reduction of the effective permeability. Evidently, reduction in permeability results in a poor productivity of the wells. Generally, well testing techniques provide the skin factor as an overall measure of formation damage [29].

It is of importance to optimize techniques that treat these impairments. Not only for the reason that formation damage occurs in almost every field operation but also for the significant magnitude of damage inflicted on well productivity. The magnitude of formation damage is sensible in the production performance of a well [28].

Matrix acidizing is a primary technique to remove these near wellbore impairments. It is, unsurprisingly, a technique to dissolve the formation matrix by injecting the appropriate acids. Several variables need to be taken into account for an optimal acidizing treatment (i.e. temperature, injection rate and target formation type). Matrix acidizing can be distinguished from other techniques by the pressure of the injected acid, since the pressure of the injected acid is below the formation failure pressure. Consequently, the formation is not fractured due to the injection of the acid [9].

[1] "A wellbore is a hole drilled in the ground in order to look for or extract natural resources such as oil and gas.", from Collins Dictionary.

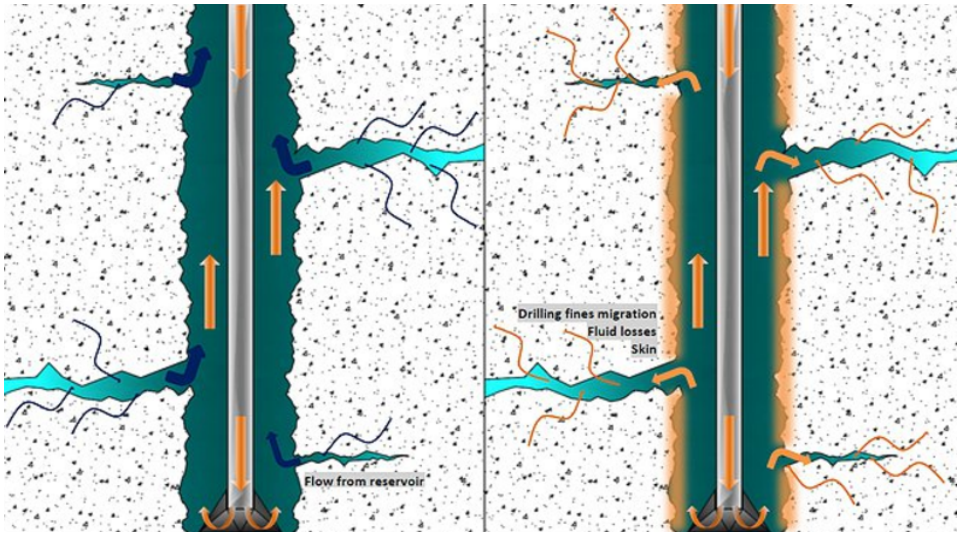

Figure 1.1: Over balanced (right) and under balanced drilling (left). Fines migrate from the formation and into the formation, respectively [24].

In general the target formations are divided into (1) Sandstone and (2) Carbonate. Below, a brief description for each type is provided.

- Sandstone: Classifying sandstone is not straightforward. There are multiple descriptive classification proposals. The proposal offered by Mc Bride states a descriptive classification of sandstones (exclusive of carbonate and volcaniclastic sandstones) based on the composition of framework grains [3]. Among others, this classification is of interest because it is based on the composition of the grains that compose the framework. This provides the possibility to target formations with effective acids. For instance, if a sandstone formation is classified based on a dominance in quartz minerals, it is not effective to inject hydrochloric acid for acidizing treatment purposes (see Table 1.1).

  Referring to a paper published in 1970 [7], the sandstone and carbonate reserves in large fields were approximated to be respectively 68% and 32%. Self evidently, it is of great importance to study matrix acidizing in both sandstones and carbonates. However, the scope of this thesis is solely focused on carbonate matrix acidizing.

- Carbonate: Similar to sandstone, descriptive classification proposals based on grain composition are favorable to determine potential effective acids. These classification models state that carbonate is dominantly composed out of carbonate minerals [11]. Carbonate minerals are those minerals containing the carbonate ion (CO_3^{2-}). As displayed in Table 1.1, both hydrofluoric acid (HF) and hydrochloric acid (HCL) are reactive with the carbonate matrix [22]. This reactivity can be beneficial to a certain extend. Reactivity of these acids is increasing with increasing pressure and temperature [12]. If the reactivity of the acid becomes too strong, several disadvantages can occur [2].

In general, temperature and pressure increase with increasing vertical depth. The corresponding increase in reactivity of conventional acids (e.g. HCL and HFL) can lead to highly accelerated corrosion [16]. Apart from corrosion, high reactivity degrades the efficiency of the carbonate matrix acidizing procedure. The principle behind the degradation will be addressed in this thesis.

AkzoNobel offers a solution for the summarized complications in the form of an unconventional acid. This product, Dissolvine® Stimwell, consists out of chelating agents. The product is less reactive at high pressure and temperature. Apart from reactivity benefits, the product consists out of the GLDA chelating agent which is readily biodegradable and offers a high solubility over a wide pH range [2].

The product has already been tested extensively both at pore and core scales. However, the behavior of the acid at a more extensional (i.e., reservoir and near wellbore) scale has not been tested yet. This thesis provides a framework for building a fully coupled acidizing treatment simulator at the "larger scale" i.e., (near wellbore). The term "larger scale" is introduced as an intermediate scale between core and reservoir scale. The simulator is tailored for the characteristics of the reaction kinetics corresponding to the Dissolvine® Stimwell acid.

Multiple challenges occur by moving from the core scale to a more extensional scale (i.e. "larger scale"). The simulator –developed in this thesis from scratch– is developed in Matlab - Mathworks© . Discretization was performed according the local mass-conservative Tow-Point-Flux-Approximation (TPFA) finite volume scheme along with first-order upwind scheme for transport convection on equidistant structured Cartesian grids.

Table 1.1: Solubility of minerals in acid [22]

Mineral	Acid	
	HF	HCL
Quartz (sandstone)	No	Very low
Calcite (Carbonate)	High	High
Dolomite (Carbonate)	High	High
Ankerite (Carbonate)	High	High
Siderite (Carbonate)	High	High

CHAPTER 2

CARBONATE ACIDIZING TREATMENT

Carbonate matrix acidizing is characterized by a specific physical phenomena. This phenomena becomes visible if the reactivity of the acid and the injection rate (i.e. acid influx) pass a certain threshold. At this point highly conductive flow channels start to grow. These flow channels are known as wormholes [21]. Wormhole efficiency curves are a convenient way to observe the transition from uniform face dissolution to fingering phenomena (i.e. wormholes).

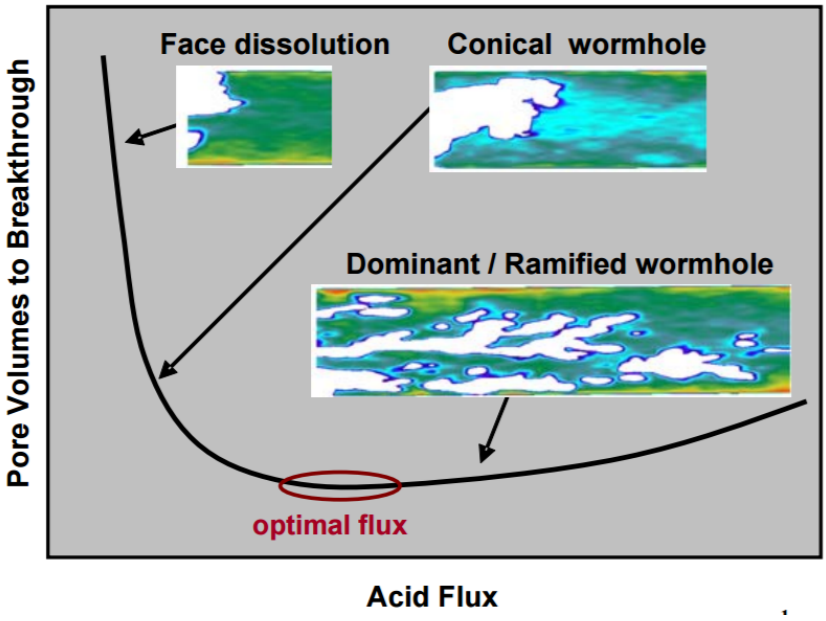

Figure 2.1: Wormhole Efficiency Curve for Quarried Carbonate (Dolomite) [15].

Figure 2.1 consists of an efficiency curve acquired from experiments performed at core scale [15]. As a function of acid injection, multiple phases are visible. Initially, the dissolution occurs uniformly. With increasing injection rates (keeping T = cte.), conical wormholes and subsequently dominant/ramified wormholes start to form. The formation of Wormholes is favorable for well stimulation purposes since the generated wormholes can function as highly conductive flow channels [1]. An optimal scenario would be, to generate the thinnest wormholes with the deepest penetration into the formation while spending a minimum amount of acid [23]. This scenario is displayed in the efficiency curve (Figure 2.1) as the optimal influx. Also note that pore volume to breakthrough on the y axis of the efficiency curve indicates the amount of injected fluid needed for a wormhole to reach the outlet. This already provides a slight indication that matrix acidizing experiments are predominantly performed at the core scale.

After a matrix acidizing experiment, the core is scanned using computed tomography (CT). The results from the computed tomography give a clear visualization of the propagation of wormholes into the formation. Figure 2.2 shows the high resolution images of three acidized Indiana Limestone cores along the worm holing efficiency curve at low, optimum and high acid influx, respectively [15].

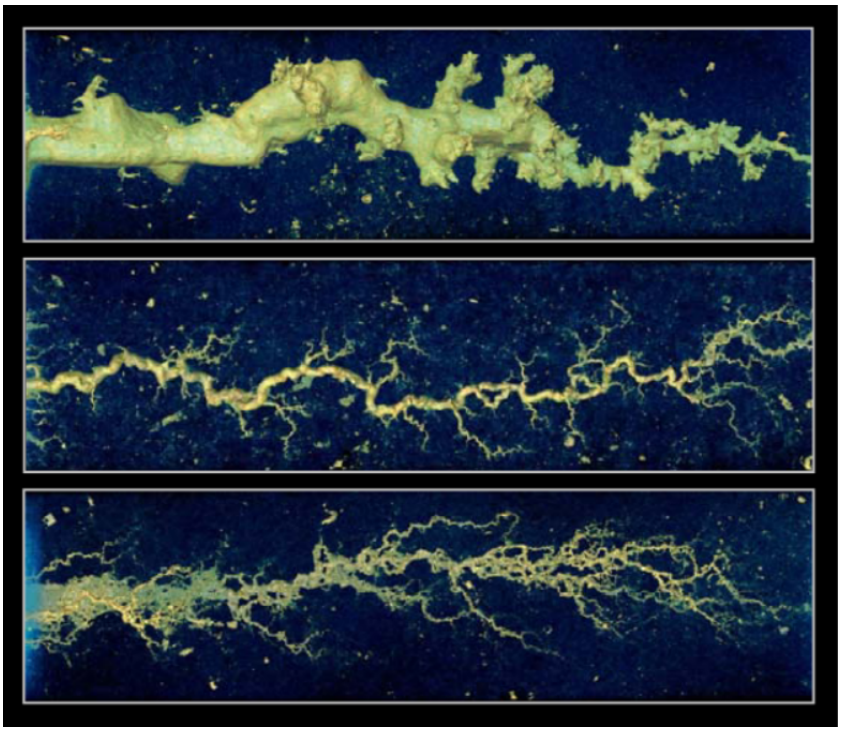

Figure 2.2: High-Resolution CT images of Acidized Core Plugs under Low (top), Optimum (middle), and High (bottom) acid influx conditions. The core plugs consist of Indiana Limestone [15].

2.1 Chemical reaction

The formation of wormholes originates from the chemical reactions at the pore scale. Capturing the correct reaction kinetics at this scale is of importance for the developed simulator. The acid-rock interaction can be limited by the mass transfer or by the reaction kinetics [17]. Experimental research performed by AkzoNobel indicates that the reaction between the Dissolvine® Stimwell product and the carbonate matrix occurs almost instantaneous. Which makes it reasonable to assume that the reaction between Dissolvine® Stimwell and carbonate is mass transfer limited.

2.1.1 Conventional chemical reaction

The most frequently used conventional acids, during a carbonate matrix treatment, are hydrochloric (HCl) and hydrofluoric acid (HF). These acids posses a high reactivity with carbonate minerals [16]. However, in a high temperature domain these acids become so reactive that they cause corrosion and impair the wormhole growth process. Nearly all the acid is spent close to the wellbore due to this high reactivity [19]. A higher injection rate is needed to proceed from the face dissolution stage to the formation of wormholes (Figure 2.1). The reaction mechanisms between the main carbonate minerals and the conventional HCl and HF acids are listed in Table 2.1.

Table 2.1: Reaction mechanisms carbonate minerals with conventional acids [8].

Mineral	Reaction
Dolomite	$4HCL + CaMg(CO_3)_2 \rightarrow CaCl_2 + MgCl_2 + 2CO_2 + 2H_2O$
Calcite	$2HCL + CaCO_3 \rightarrow CaCl_2 + CO_2 + H_2O$
Dolomite	$2HF + CaCO_3 \rightarrow CaF_2 + CO_2 + H_2O$
Calcite	$2HF + CaMg(CO_3)_2 \rightarrow CaF_2 + MgF_2 + 2CO_2 + H_2O$

2.1.2 Dissolvine® Stimwell chemical reaction

The chelating agent GLDA in the Dissolvine® Stimwell product is responsible for the dissolution of the metal containing carbonate minerals [2]. Chelating agents are widely employable, apart from well stimulation purposes, they serve solutions for several problems. For instance, the mitigation of scale forming in boilers, heater tubes and flow lines (i.e flow assurance) [13].

The GLDA chelating agent is a glutaminic diacetic acid. GLDA has four carboxylic acid groups and combined with a centralized nitrogen atom these carboxylate groups provide strong multiple bonds with di- and trivalent metal ions [14]. One of the unionized forms of the GLDA molecule is the $GLDA - Na_4$ molecule. The structure formula of this molecule is displayed in Figure 2.3.

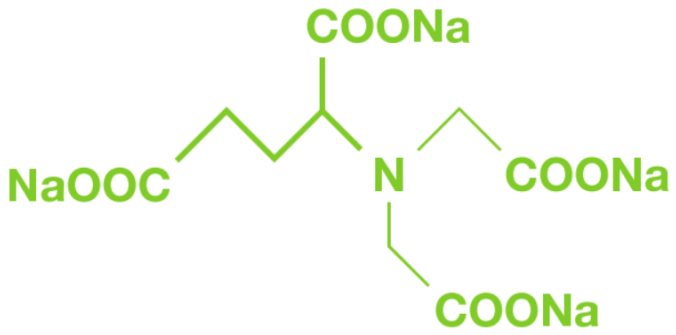

Figure 2.3: Structure formula of the $GLDA - Na_4$ molecule [2].

The Dissolvine® Stimwell product is readily biodegradable since the GLDA molecule is based on the food-approved natural amino acid salt, mono sodium L-glutamate (MSG) [2]. More properties of the main component of the Dissolvine® Stimwell product (i.e. GLDA agent) can be found in Table 2.2.

Aminopolycarboxylic acids, such as GLDA, undergo a stepwise loss of protons to reach their fully ionized state [6]. GLDA dissociates in four steps since the molecule has four carboxylic acid groups (Figure 2.3). The dissociation reactions are given by equations (2.1) to (2.4), respectively, i.e.

$$H_4Y \leftrightarrow H_3Y^- + H^+ \tag{2.1}$$

$$H_3Y^- \leftrightarrow H_2Y^{2-} + H^+ \tag{2.2}$$

$$H_2Y^{2-} \leftrightarrow H_Y^{3-} + H^+ \tag{2.3}$$

$$HY^{3-} \leftrightarrow Y^{4-} + H^+. \tag{2.4}$$

Here, H_mY^{m-n} represents the chelating agent molecule, and m hydrogens are those of the carboxylic acid group [6]. The dissociation process of GLDA is depended on the pH. This dependency is illustrated in Figure 2.4.

Table 2.2: Molecule details $GLDA - Na_4$ molecule [2]

CAS No	51981-21-6
Chemical formula	$C_9H_9NO_8NA_4$
Molecular weight	3511.1 g/mol

At a pH of 8, the GLDA molecules start to reach the fully ionized state. The protons that are formed during the dissociation reactions (equations (2.1) to (2.4)), react with the carbonate minerals/matrix. Three surface reactions occur simultaneously. The reactions are formulated as

$$H^+ + CaCO_3 \leftrightarrow Ca^{2+} + HCO_3^- \tag{2.5}$$

$$H_2CO_3 + CaCO_3 \leftrightarrow Ca^{2+} + 2HCO_3^- \tag{2.6}$$

$$H_2O + CaCO_3 \leftrightarrow Ca^{2+} + HCO_3^- + OH^-. \tag{2.7}$$

One of these equations can be dominant. This dominance is depended on the pH (Figure 2.4) and the partial pressure of CO_2 [10].

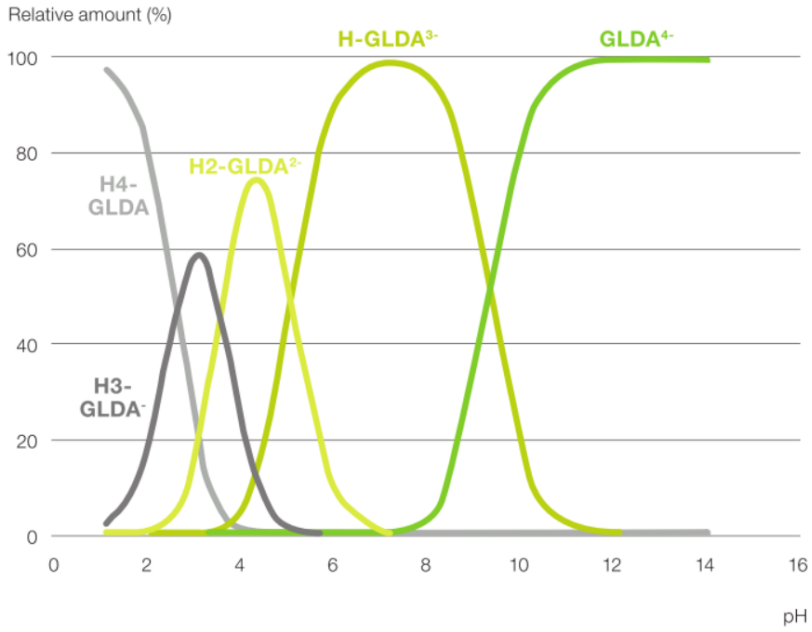

Figure 2.4: pH dependency of the GLDA dissociation process [2].

CHAPTER 3

SIMULATION STRATEGIES

3.1 Governing equations

The governing equations are used to simulate the injection of the Dissolvine® Stimwell acid at the "Larger scale". The larger scale is a newly introduced term, which refers to an intermediate scale between the core and the reservoir scale (i.e., near-wellbore region). The reaction rate $R(C)$ is modeled as

$$k_c(C_f - C_s) = R(C_s), \tag{3.1}$$

where k_c,C_f and C_s are the local mass transfer coefficient, acid concentration in the fluid phase, and the acid concentration at the solid-fluid interface, respectively [17]. The porosity evolution can be also modeled [17] as a function of the reaction rate as

$$\frac{\partial \phi}{\partial t} = \frac{R(C_s) a_v \alpha}{\rho_s}. \tag{3.2}$$

This equation consists out of the porosity (i.e. ϕ), interfacial area per unit volume (i.e. a_v), reaction rate (i.e. $R(C)$) and rock density (i.e. ρ_s). An empirical relationship is used to determine the change in interfacial surface area per unit volume [21], i.e.,

$$\frac{a_v}{a_o} = \frac{\phi}{\phi_o} \frac{\phi(1-\phi_0)}{\phi_0(1-\phi)}^{-\beta}. \tag{3.3}$$

Here, β is a constant representing the dependency on the pore structure. The continuity equation is written for an incompressible single phase fluid with no additional source term, i.e.,

$$\frac{\partial \phi}{\partial t} + \nabla \cdot u = 0. \tag{3.4}$$

A convection diffusion equation [17] is now solved for the concentration evolution in the medium, i.e.,

$$\frac{\partial(\phi C_f)}{\partial t} + \nabla \cdot (u C_f) = D_e \nabla \cdot (\phi \cdot \nabla C_f) - a_v \, R(C_f), \tag{3.5}$$

where the dispersion tensor is denoted as D_e. An empirical relationship is used to compute the permeability change [1] as

$$\frac{K}{K_0} = \frac{\phi}{\phi_0} \left[\frac{\phi(1-\phi_0)}{\phi_0(1-\phi)} \right]^{2\beta}, \tag{3.6}$$

where the rock permeability is denoted as K.

It is important to be emphasized that due to the creation of the wormholes, here, the coupled Darcy-Stokes equation –as described in the Brinkman equation– is used as the momentum equation [18], i.e.,

$$\nabla p = -\frac{\mu}{K} u + \mu \nabla^2 u, \tag{3.7}$$

where μ is the dynamic viscosity. In general, the viscosity in the Darcy term can be different than the viscosity of the Stokes term; based on the coupling condition at the contact surface of the free-flow and porous-medium flow; however, in this work they are taken as the same quantities.

The presented formulations govern the coupled system of equations for the unknowns. The simulation strategy should develop a coupling consideration in order to obtain all unknowns. These coupling approaches are mainly classified into (1) sequential and (2) fully-implicit (simultaneous) coupling approached. Next, the description and implementation of the two approaches are presented. Numerical results are then presented in the next Chapter.

3.2 Sequential simulation strategy

The initial approach for the newly developed simulator comprises a sequential strategy, i.e., a “step-by-step” solution strategy for the unknowns near the wellbore domain.

Figure 3.1 illustrates the steps involved in such a sequential startegy. More precisely, such a simulator would consist of five steps, which are chained within an outer iterative loop. Below, each step is being described in more detail.

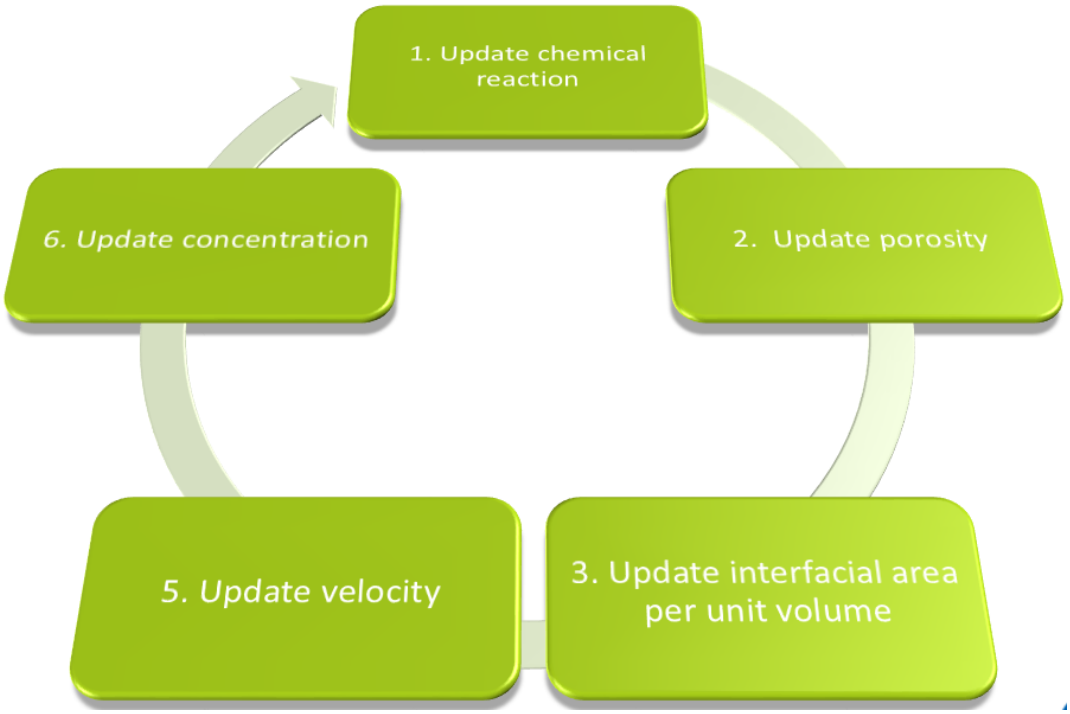

Figure 3.1: An overview of the sequential simulation strategy, where each unknown is being solved in a separate stage and the blocks are coupled through an outer loop. The main loop consists out of five steps.

Step 1: Update chemical reaction "$R(C_f)$"

The sequential loop starts with the reaction kinetics at the pore scale. Based on the conservation of mass, as shown in Figure 3.2, the reaction kinetics balances the amount of acid transferred from the fluid phase to the surface and the amount reacted at the surface [20]. The Dissolvine Stimwell acid entails high reaction rates. Therefore, the reaction kinetics for this acid are assumed to occur instantaneously. This means that the concentration of acid at the solid interface is approximately 0 (i.e. $C_s \approx 0$) [20], i.e.,

$$k_c * C_f = R(C_f). \tag{3.8}$$

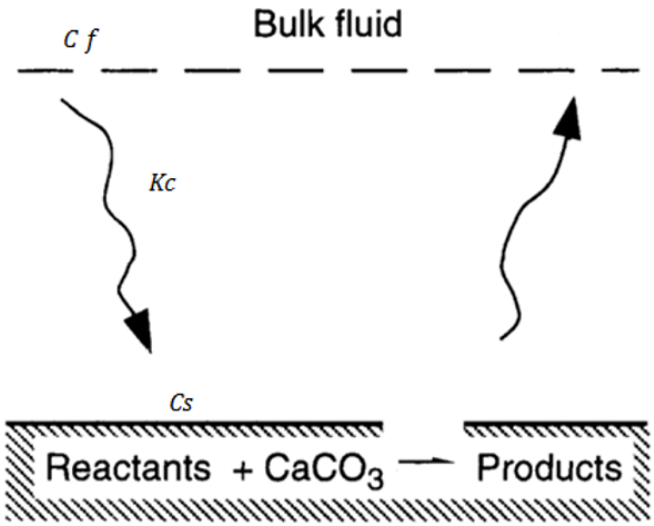

Figure 3.2: Acid propagates from the pore to the solid-fluid interface where it reacts. Note that for the Akzonobel acid (i.e., Dissolvine® Stimwell) it is assumed that $C_s \approx 0$. The figure is taken from [23].

.

Step 2: Update porosity "ϕ"

The reaction kinetics are computed as a function of the local mass transfer coefficient and acid concentration in the fluid phase for the initial time step (i.e. at t = 0). Subsequently, it becomes possible to determine the porosity at the next time step. The porosity evolution is formulated as Equation (3.2) [17]. The rock density (i.e. ρ_s), acid dissolving power (i.e. α) and interfacial surface area per unit volume (i.e. a_v) must be predefined (i.e., they are input parameters of this stage).

Step 3: Update interfacial area "a_v"

The porosity starts to increase over time as result of ongoing chemical reactions. If carbonate minerals start to dissolve, the interfacial surface area per unit volume starts to vary. The interfacial surface area per unit volume for the succeeding time step is related with porosity according to Equation (3.3) [17].

Step 4: Update velocity "u"

Mass conservation equation can be written as Equation (3.4). Since there is no source term, the acid-brine mixture is incompressible and the porosity is changing over time.

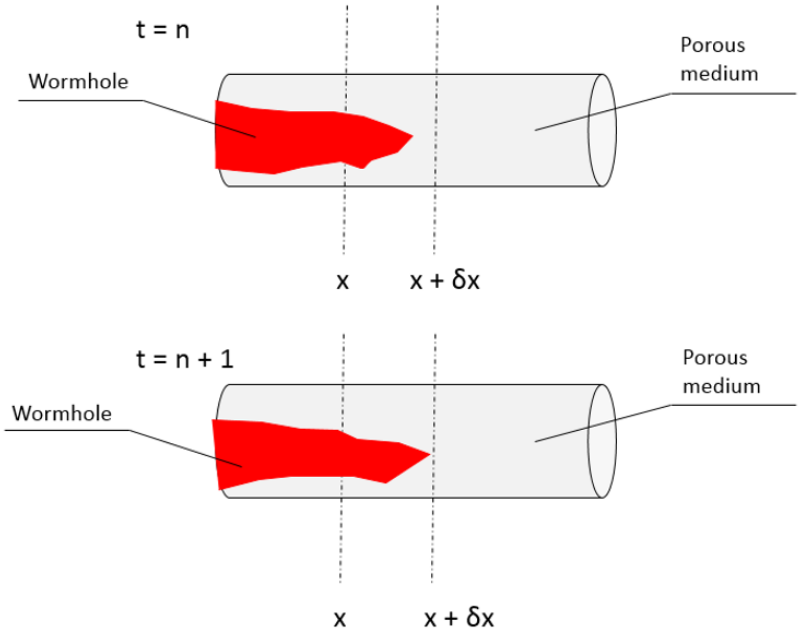

Figure 3.3: The velocity field is directly coupled with the porosity evolution over time by mass conservation.

Step 5: Update acid concentration "C_f"

The acid is transported trough the domain by convection and diffusion. This convection-diffusion problem is formulated as Equation (3.5) [17]. The reaction kinetics (i.e. $R(C_f)$) represent a sink term. Porosity depends on the acid concentration as expressed in Equation (3.2). Hence, Equation (3.5) is non linear. The equation is therefore linearized with a newton linearization scheme [4], which then results in solving for concentration in a residual-form iterative procedure. Initially, a guess is made for the concentration (i.e. $C_f^\nu \leftarrow C_f^n$). Subsequently, the residual is computed after linearizing equation 3.5. Once the residual is computed the system $J^\nu \delta C_f^{\nu+1} = -R^\nu$ is solved for $\delta C_f^{\nu+1}$. In the next step, the initial guess is updated with $\delta C_f^{\nu+1}$. The system converges (i.e. Step 4 in Figure 3.1) if $\delta C_f^{\nu+1}$ is approximately zero (i.e. error margin of 10^{-6}). If this is not the case, the loop is iterated until the system converges. After converging, the system succeeds to the next time step. An overview of this iterative procedure is illustrated in Figure 3.4.

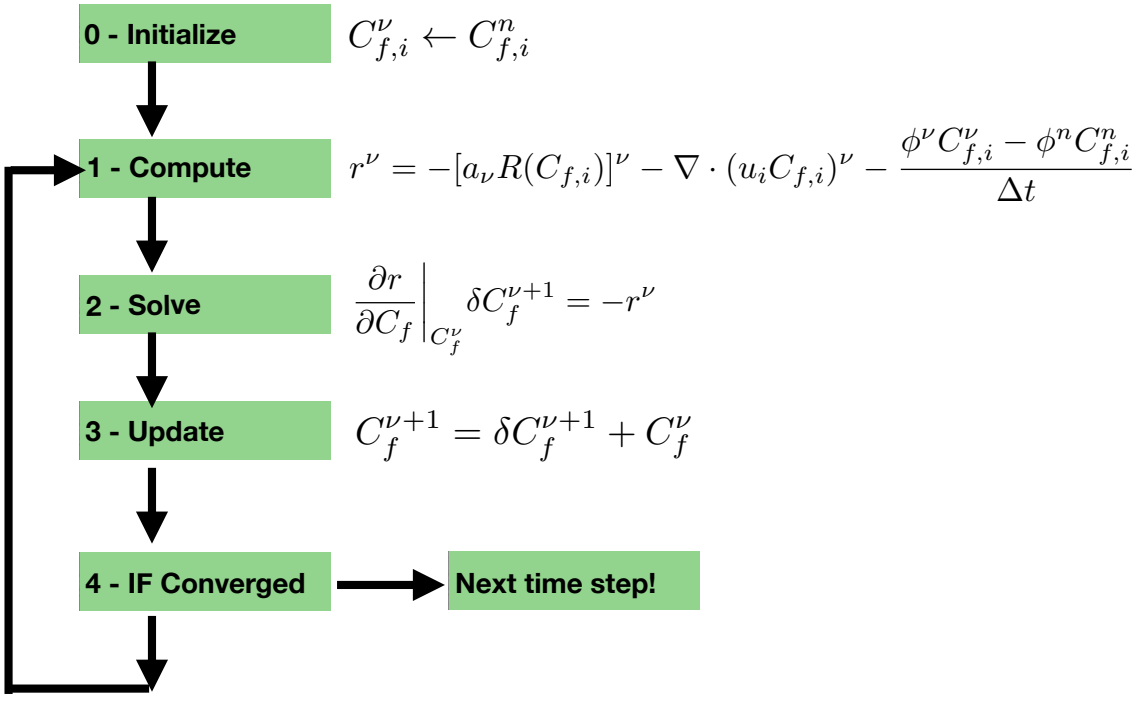

Figure 3.4: Inner iteration loop for solving for the acid concentration. Note that convective terms are solve using a first-order upwind scheme, and that diffusion is neglected (due to the grid sizes). This loop is performed at Step 5 of the sequential simulation approach.

Once the outer-loop (consisting of the 5 mentioned steps) is converged; the secondary variables are updated. The choice of having velocity or pressure as the primary variable depends on the dimension of the domain. While for 1D domains one can use velocity as the primary variable (since its vectorial space reduces to scalar u_x unknown), for higher dimensional domains a pressure equation needs to be derived to replace the continuity equation at Step 4. If the velocity is taken as the primary unknown, pressure will be updated using Brinkman's formula. An illustration of the Brinkman's formula is provided in Figure 3.5. Brinkman's formula combines the Darcy and Stokes formulations in a unified way to contribute to the total pressure drop in a porous media which consists of sub-domains with channel-flow (i.e., Stokes regime). The left and right sub-figures in Figure 3.5 illustrate the cases when the Brinkman's formula reduces to Darcy (when K is low) and Stokes (when K is very high) [18].

If the pressure is used as the primary unknown, one should substitute the Brinkamn's equation into the continuity (mass-balane) equation so that an equation for pressure is obtained. Then this equation is solved for pressure at Step 4. In each outer-loop, the velocity is being

updated, once the pressure is updated, in a post-processing stage using the Brinkamn's formula. This approach is more consistent with classical sequential reservoir simulation methods, in which a pressure equation is obtained by substituting Darcy's law into the mass balance (continuity) equation.

It is known that the sequential strategy is stable when the coupling between the unknowns is not strong. However, when the coupling terms (dependency of the unknowns) is strong, fully-implicit (FIM) methods are more advantageous. Next, a FIM framework is developed in order to allow for general coupling strength between the unknowns. Note that this FIM simulator is being used as the reference of most studies performed in this thesis.

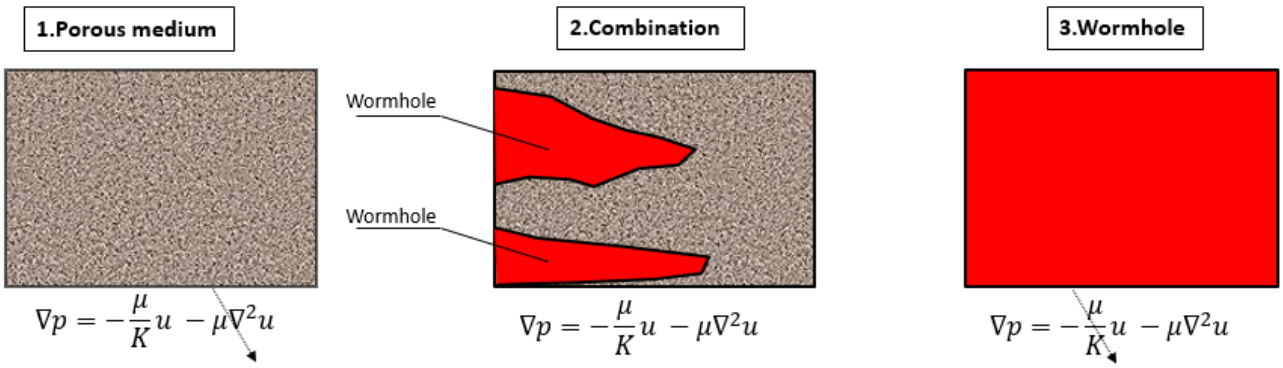

Figure 3.5: The Darcy-Stokes equation captures the pressure calculation in both the wormholes and the porous medium.

3.3 FIM solver

Simulation of acidizing treatment at the "larger scale" (i.e. intermediate scale between core and reservoir scale) is complex. This complexity can be further enhanced by strong coupling between the reaction kinetics and the fluid dynamics. A fully implicit (FIM) approach allows for more stable and robust treatment of the coupling terms [5].
The governing equations that comprise the sequential solver are re-written into a residual form as following, i.e.,

$$R_1 = \frac{\partial(\phi)}{\partial t} - \frac{k_c C_f a_v \alpha}{\rho_s} \tag{3.9}$$

$$R_2 = \nabla \cdot (u) + \frac{\partial \phi}{\partial t} \tag{3.10}$$

$$R_3 = \frac{\partial(\phi C_f)}{\partial t} + \nabla \cdot (u C_f) + k_c a_v C_f. \tag{3.11}$$

Note that if pressure is taken as primary unknown, Equation (3.10) will be replaced by a pressure equation. The interfacial area per unit volume is a function of porosity as formulated in Equation (3.3). The local mass transfer coefficient is assumed to be constant. The convective term on the RHS of Equation (3.11) is discretized according to a first order upwind scheme.

Convection causes the acid-brine mixture to propagate into the high permeable regions. For a heterogeneous carbonate rock this results into fingering (i.e. wormhole formation). Please note that the diffusive term is neglected in Equation (3.11), due to the time and grid-size scales and the dominance of the convective term in the process of wormhole formation.
The reaction kinetics, represented by Equation (3.9), are rewritten as

$$R_1 = \frac{\partial(\phi)}{\partial t} - A(1-\phi)C_f, \tag{3.12}$$

where the constant A is introduced as the acid tuning factor, i.e.

$$A = \frac{K_c \alpha a_{v,0}}{\rho_s(1-\phi_0)}. \tag{3.13}$$

This factor makes it possible to implement the acid dissolving power.
For a one dimensional case, where velocity is taken as the primary unknown, the three derived residuals are functions of all the three main unknowns. This makes it possible to solve for all unknowns, i.e., C_f, ϕ and u simultaneously. The pressure and permeability can be computed in a post processing phase, similar to the sequential approach.

However, as mentioned before, a different approach is required for 2 and 3 dimensional cases. Since, in these cases the extra velocity components are additional unknowns (i.e., velocity is a vector of unknown). Therefore, a pressure equation is derived such that the system is well posed. In this case, the Brinkman equation is used to relate the velocity with the pressure. The FIM system is then derived for p, C_f and ϕ as the main unknowns. Subsequently, the obtained pressure is used (after each Newton loop) to compute the velocity in a post-processing stage. An overview of this approach is provided in Figure 3.6.

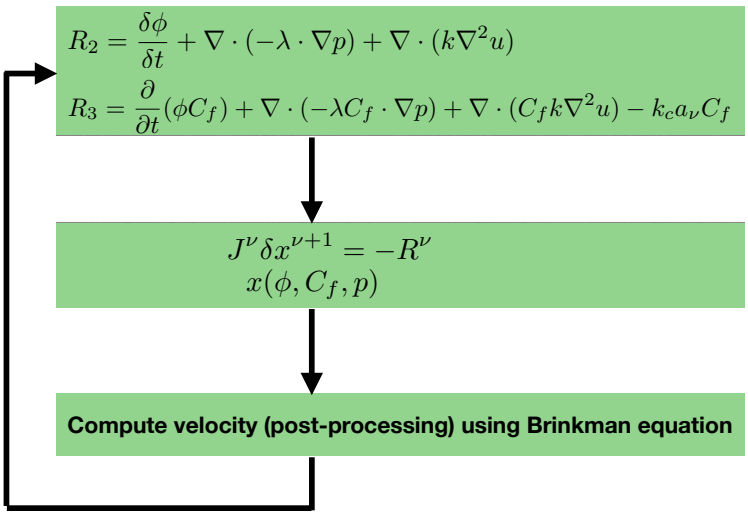

Figure 3.6: Pressure-dependent residual terms for the case where pressure is taken as the primary unknown. Note that velocity is being updated inside the Newton loop, once the pressure is being updated in the FIM system.

It is important to re-iterate that the FIM system approximates the non-linear residual R^{n+1} through iterative procedure based on the Newton's lemma, i.e.,

$$R^{n+1} \approx R^\nu + \sum \frac{\partial R}{\partial \xi}\Big|^\nu \delta\xi^{\nu+1}, \tag{3.14}$$

which can be stated as

$$R^{n+1} \approx R^{\nu+1} = R^\nu + \frac{\partial R}{\partial \phi}|^\nu \delta\phi^{\nu+1} + \frac{\partial R}{\partial C_f}|^\nu \delta C_f^{\nu+1} + \frac{\partial R}{\partial p}|^\nu \delta p^{\nu+1} \tag{3.15}$$

for our system. Finally, the linear system is obtained in the form of

$$\begin{bmatrix} \frac{\partial R_1}{\partial \phi}|^\nu & \frac{\partial R_1}{\partial C_f}|^\nu & \frac{\partial R_1}{\partial p}|^\nu \\ \frac{\partial R_2}{\partial \phi}|^\nu & \frac{\partial R_2}{\partial C_f}|^\nu & \frac{\partial R_2}{\partial p}|^\nu \\ \frac{\partial R_3}{\partial \phi}|^\nu & \frac{\partial R_3}{\partial C_f}|^\nu & \frac{\partial R_3}{\partial p}|^\nu \end{bmatrix} \begin{bmatrix} \delta\phi^{\nu+1} \\ \delta C_f^{\nu+1} \\ \delta p^{\nu+1} \end{bmatrix} = - \begin{bmatrix} R_1^\nu \\ R_2^\nu \\ R_3^\nu \end{bmatrix}. \tag{3.16}$$

Note that the convective terms in the transport equation are obtained using an upwind scheme.

CHAPTER 4

TEST CASES

4.1 2D Test Case

The fully implicit model is used to model a two dimensional (2D) test case. The Stimwell product is injected under a constant horizontal velocity (i.e. $u_L = cte.$). The right boundary condition comprises of the reservoir pressure (i.e. p_R). There is assumed to be no flow trough the top and bottom boundaries of the domain. In this test case the Dissolvine® Stimwell product is injected into a 5×5 meter carbonate block. A heterogeneity is imposed by populating the carbonate block with porosities drawn from a normal distribution with a mean of 0.12 and a standard deviation of 0.01. The input data for this particular test case is presented in Table 4.1.

Table 4.1: Input data for 2D test case.

Input	Value
ϕ	0.09-0.15 [−]
Lx	5 [m]
Ly	5 [m]
p_R	20 [Bar]
u_L	9E-4 [m/s]
ρ_s	2710 [kg/m^3]
k_c	1E-7 [m/s]
α	60 [g/mol]
a_v	200 [m^{-1}]
K_0	10E-13 [m^2]
μ	1E-3 [$Pa.s$]
β	0.5 [−]

4.1.1 Concentration

The Dissolvine® Stimwell acid propagates trough the carbonate rock. A clear acid front is visible at each time step (see Figures 4.1 and 4.2). More acid gets transported trough the highly permeable wormholes. This preference in flow path is visible in Figure 4.3. The rate at which the concentration front propagates depends on several factors among which the pressure differential between the inlet and the set boundary, the acid tuning factor and the rock properties.

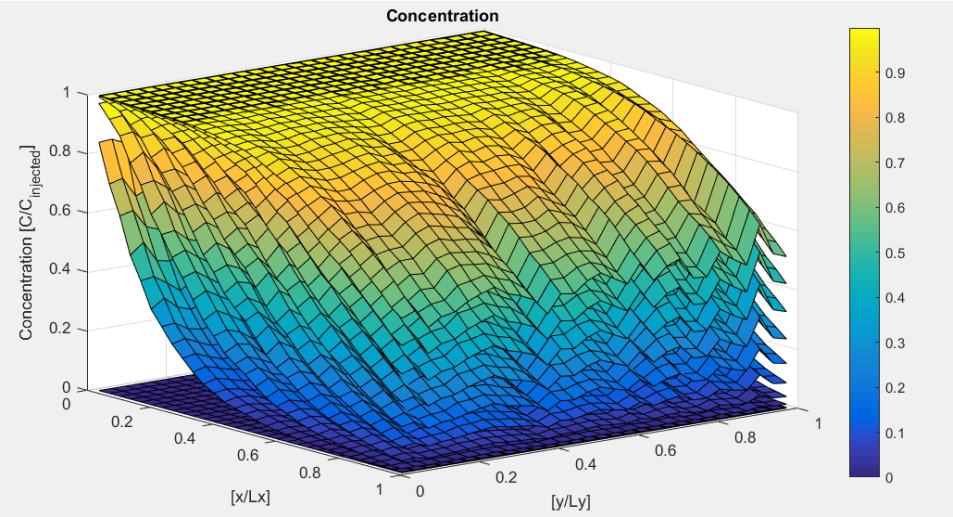

Figure 4.1: Surface plot of the concentration distribution at different time until 2 hours.

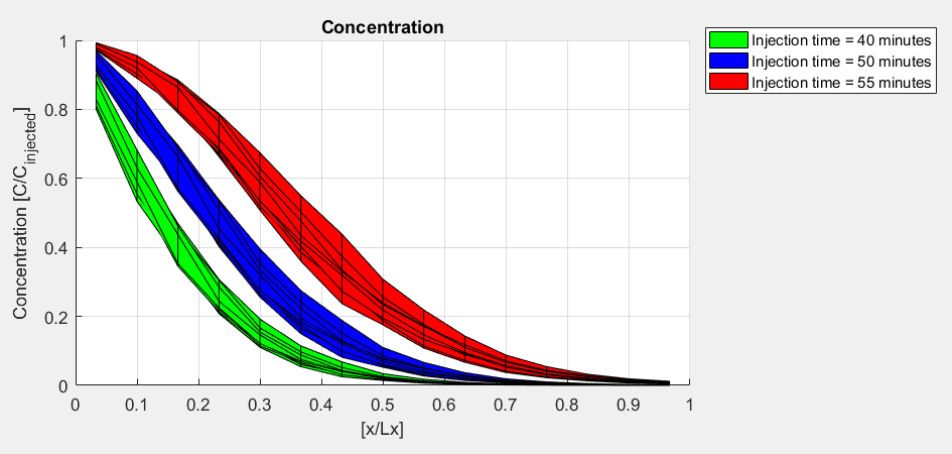

Figure 4.2: Side-view of the concentration profile at different times.

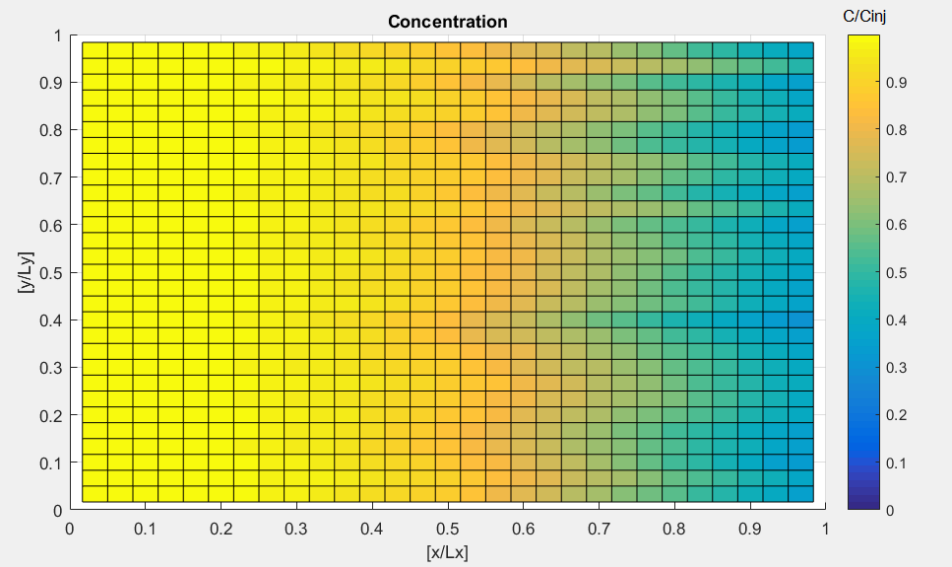

Figure 4.3: Top-view of the concentration distribution after 2 hours of injection.

4.1.2 Velocity and pressure

The horizontal velocity plot tends to reveal the presence of wormholes (see Figures 4.4 and 4.5). Several wormholes become visible near the inlet where the horizontal velocity is relatively high. Fingering and preferential flow paths are clearly visible in the top view plot (Figure 4.5). The vertical velocity is plotted in Figure 4.6. Over time the damage near the well bore gets removed, resulting in a pressure drop near the inlet (see Figure 4.7).

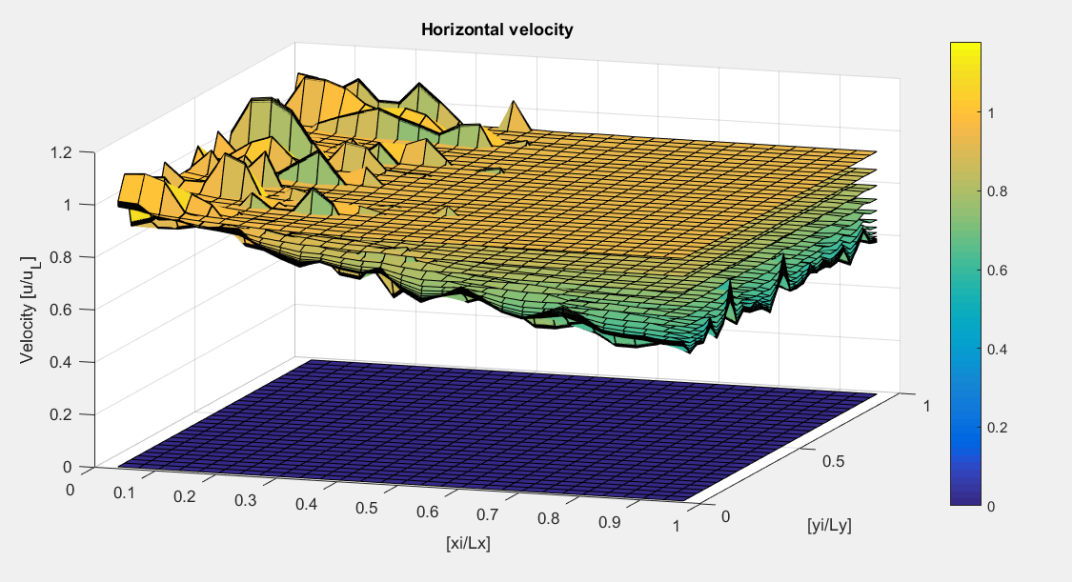

Figure 4.4: Surface plot of the horizontal velocity u_x at different times, until 2 hours of injection.

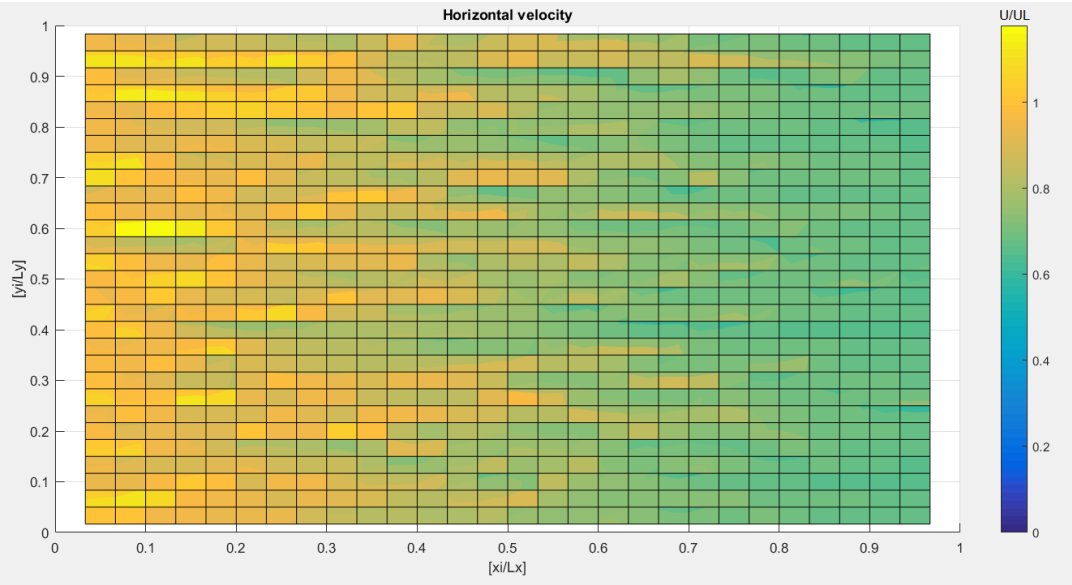

Figure 4.5: Top-view of the horizontal velocity u_x distribution after 2 hours of injection.

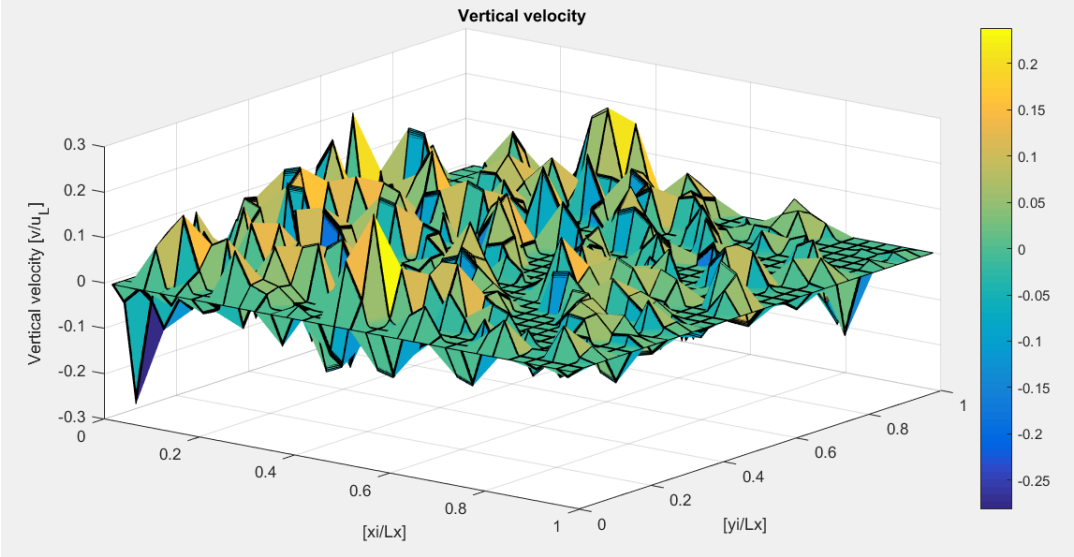

Figure 4.6: Surface plot of vertical velocity distribution u_y after 2 hours of the injection of the acid.

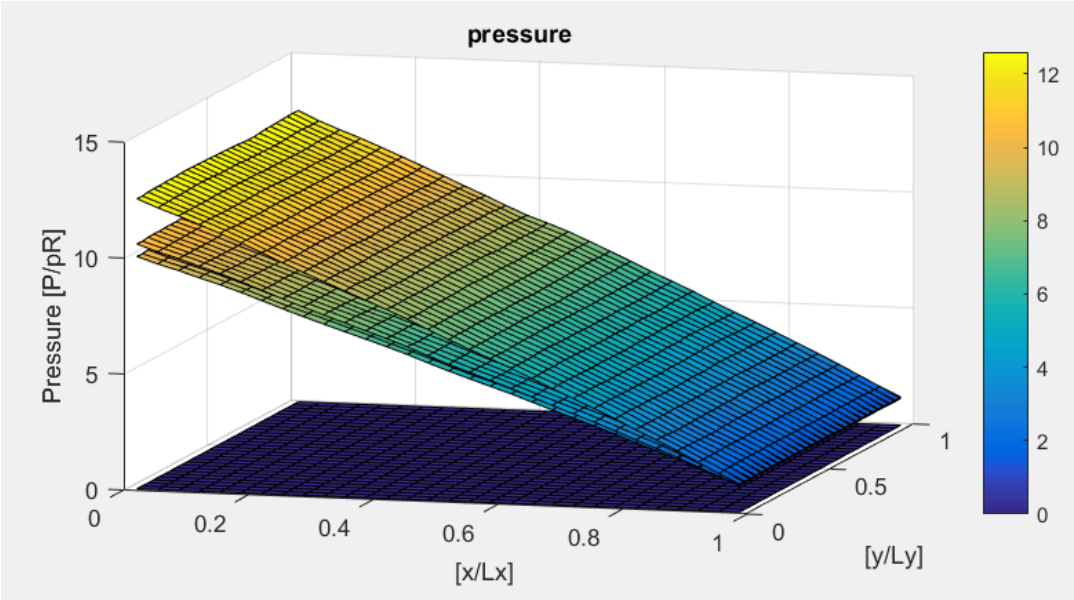

Figure 4.7: Surface plot of pressure distribution P at different times, until 2 hours of injection.

4.1.3 Porosity and permeability

The upscaled porosity results are plotted in Figure 4.8. An increase in porosity is visible. The upscaled porosity increase is felt most near the inlet. However, after approximately 40 minutes of injection the upscaled porosity starts to increase at the right boundary. Indicating that wormholes

penetrated into the carbonate rock. The porosity increase is highly depended on the acid injection rate and acid reactivity. The corresponding permeability increase is plotted in Figure 4.9.

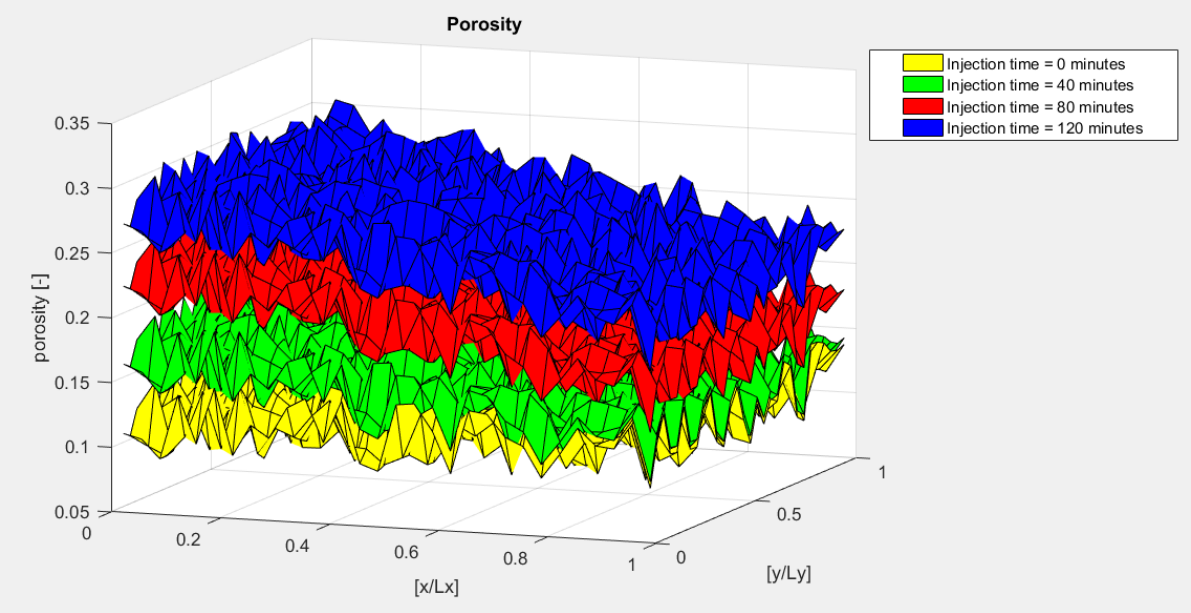

Figure 4.8: Surface plot of porosity distribution ϕ at different times, until 2 hours of injection.

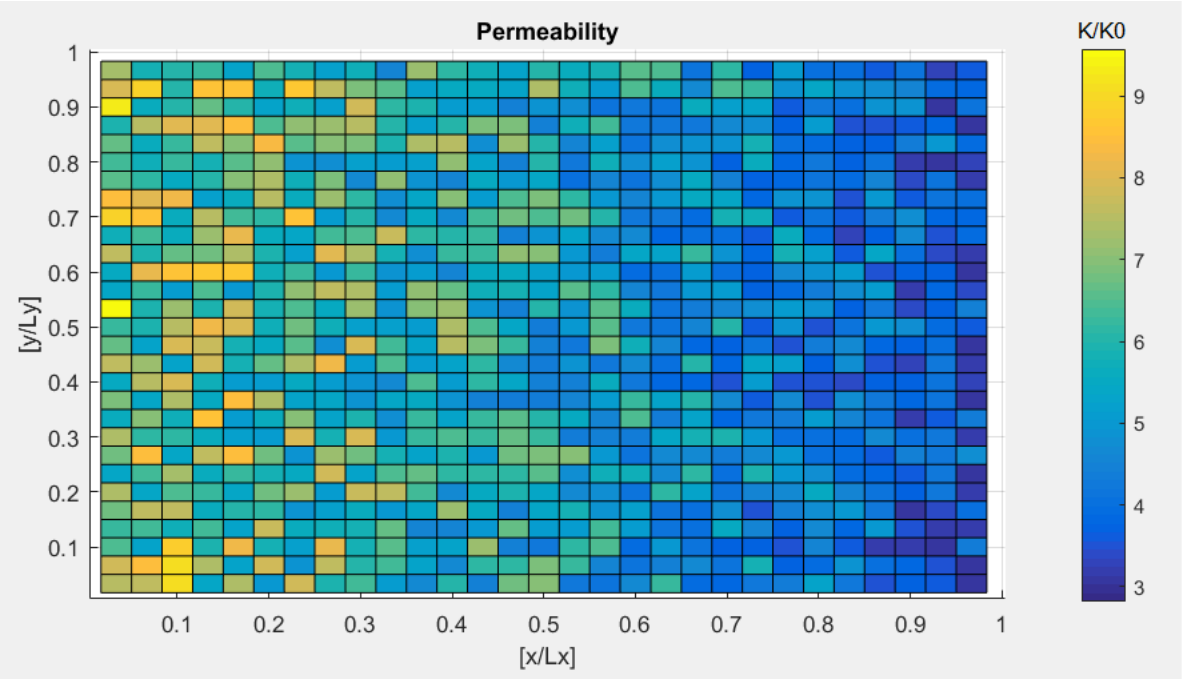

Figure 4.9: Top-view of the permeability distribution K after 2 hours of injection

CHAPTER 5

VALIDATION

5.1 Validation with experimental results at unprecedented scale

Several acidizing experiments are performed at the core scale. However, larger-scale systems must be considered if 3D wormhole characteristics are to be understood [15]. The costs of acidizing experiments at this scale are significantly high [25]. Hence, only a few experiments are conducted at this particular scale. Large scale in this context refers to an intermediate scale between the reservoir and the core scale. One of these experiments was carried out at TerraTek in Salt Lake City. This experiment was conducted using a large rock sample of up to $14ft^3$ (see Figure 5.1). The rock sample, weighing nearly 1 ton, was placed under stress levels comparable to actual subsurface conditions [15]. Subsequently, the rock was injected with a conventional HCl acid. Only the top and bottom of the large block are sealed, allowing the injected fluid to exit via the lateral boundaries of the Acidizing cell. The injection rate is adjusted to find the optimal flux, similar to the discussed efficiency curve in Chapter 2. Upon completion of the acidizing experiment, the large block is scanned using a CT system.

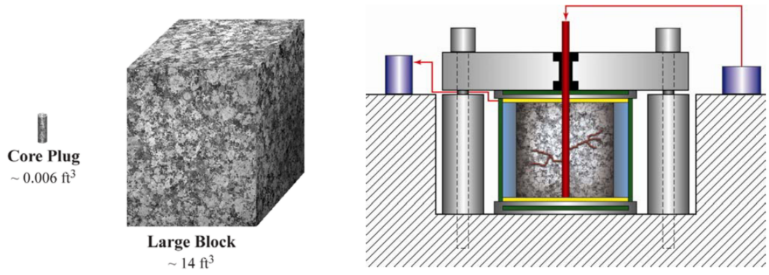

Figure 5.1: The large block is 2000 times the volume of the core plug and placed in an acidizing test cell. [15].

It is almost impossible to validate the experimental results in details of the exact configuration of the wormholes, as for the several uncertainties including the unknown heterogeneity of that specific rock sample. However, one can investigate the trend of the wormhole creation length depending on the injection rate. This would be a valuable contribution of the simulator developed in this project, as this dependency can provide important operational information for field applications.

Figure 5.2 illustrated the experimental wormhole creation dependency on the pump injection rate.

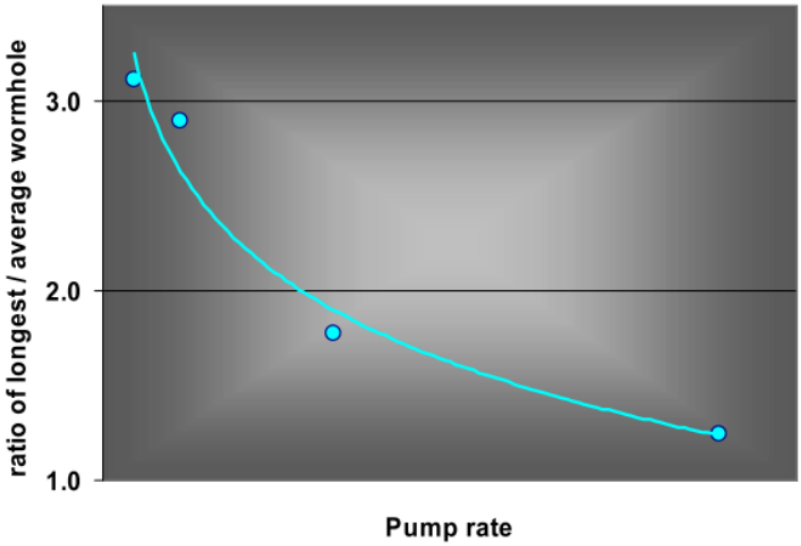

Figure 5.2: The ratio of longest to average wormhole as a function of the injection influx/pump rate regarding the large block experiment in Salt Lake City, Utah [15].

In our simulator, the porosity distribution is used to estimate the length and distribution of the wormholes. As shown in Figure 5.1, the average and longest wormholes are set to be located at $\lambda_{average} = 0.6$ and $\lambda_{longest} = 0.25$, respectively.

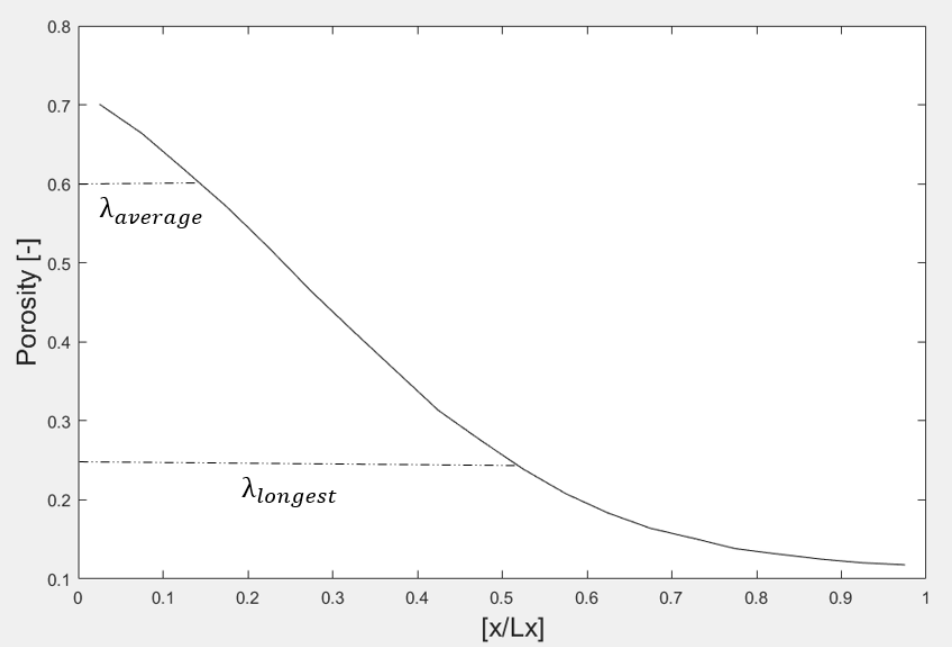

Figure 5.3: Determination of the longest and the average wormhole length based on the averaged porosity plot.

Using this approach to calculate the wormhole geometrical characteristics, and the data provided in Table 5.1, similar trend of the wormhole creation dependency on the injection flow rate is found with the developed simulator (see Figure 5.4).

Table 5.1: Input data used for validation with the experiment of [15].

Input	Value
ϕ	0.09-0.15 [−]
Lx	7 [m]
Ly	1 [m]
Lz	1 [m]
p_R	50 [Bar]
Q_L	1.5E-4 [m^3/s]
ρ_s	2710 [kg/m^3]
k_c	1E-7 [m/s]
α	100 [g/mol]
a_v	200 [m^{-1}]
K_0	10E-13 [m^2]
μ	1E-3 [$Pa.s$]
β	0.5 [−]

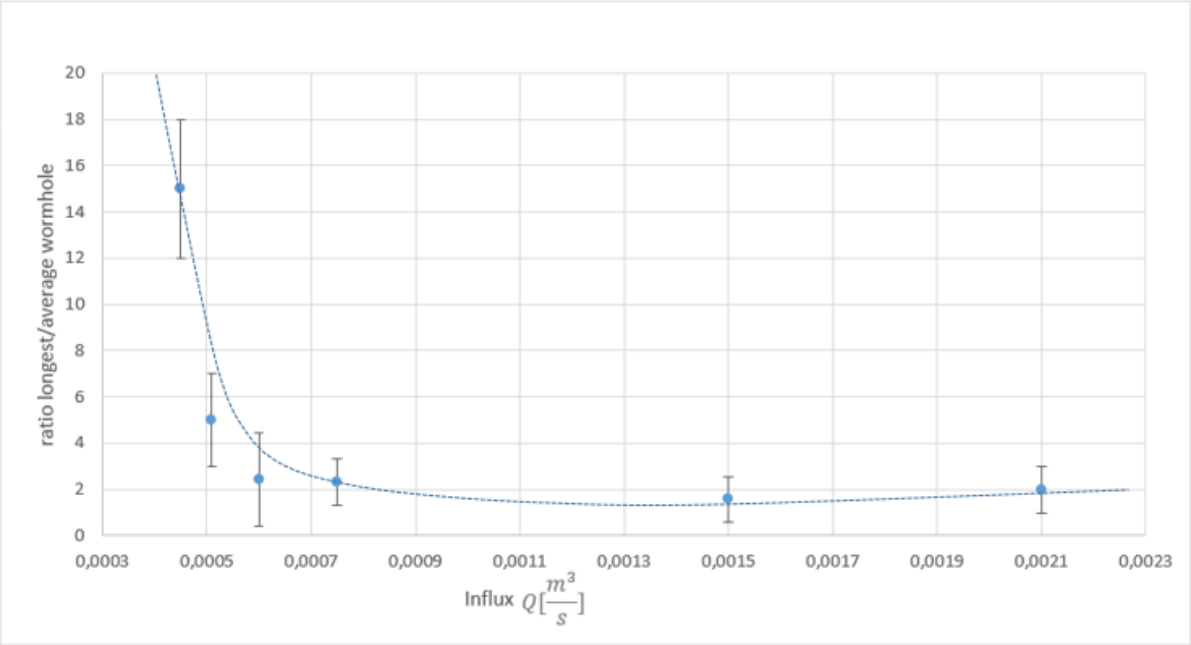

Figure 5.4: The ratio of the longest to average wormhole length as a function of the acid injection flow rate. Results obtained from the developed simulator

5.2 Validation with experimental results at core scale

At the core scale, the pore volume to breakthrough (i.e. PVBT) is an important quantity. It allows to compute the efficiency curve, which is used to identify the optimal injection rate for a particular acidizing treatment. The efficiency curve is plotted at the "larger scale" based on simulation results. The fully implicit model is used to stack the result of 50 simulations on top of each other (so as to consider the uncertainty within the initial porosity and permeability distribution). These simulations are performed on a 1D structured Cartesian grid with input data as presented in Table 5.1. The left and right boundaries are subject to Dirichlet acid influx and pressure, respectively.

If wormholes breakthrough, a highly conductive tunnel between the left and the right boundary is formed. This conductive tunnel causes the pressure at the inlet to decay significantly. A breakthrough is considered to occur if

$$\frac{\Delta P_{end}}{\Delta P_{initial}} < 10 \tag{5.1}$$

is satisfied. Under this condition the pressure difference at the inlet and the outlet is so small that the carbonate block is assumed to have tunnel-like behavior. Hence, wormhole(s) are broken through.

The initial pore volume is computed by multiplication of the porosity with the volume of the carbonate block, i.e.,

$$PV_{initial} = V \cdot \phi. \tag{5.2}$$

Here, V is the volume of the Carbonate block. The pore volume used to reach breakthrough is computed by multiplication of the breakthrough time, injection velocity and area, i.e.,

$$PV_{breakthrough} = u \cdot A \cdot t_{breakthrough}. \tag{5.3}$$

Subsequently, the pore volume to breakthrough is computed as

$$PVBT = \frac{PV_{breakthrough}}{PV_{initial}}. \tag{5.4}$$

The dissolution regimes are visible in the obtained acid efficiency curve from the simulator, as shown in Figure 5.5. At low flow rates, face dissolution is visible. Increasing the flow rate leads to conical wormholes and dominant wormholes. Additionally, Figure 5.5 provides an approximation of the optimal flux indicated by the red circle.

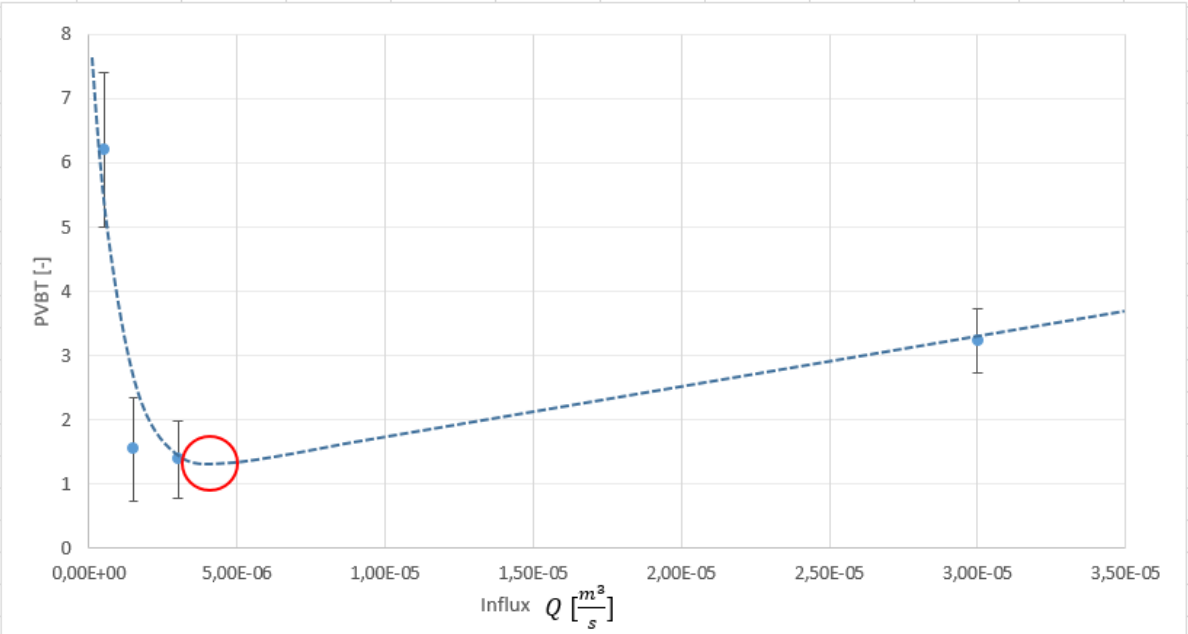

Figure 5.5: The pore volume to breakthrough as a function of acid influx. The red circle indicates the optimal flow rate. Result is obtained from the developed simulator.

CHAPTER 6

SENSITIVITY STUDY

6.1 Skin as a function of acid power

Even brief, it is still of great interest to identify the efficiency of the acidizing treatment in the productivity of the well. As such, in this chapter, this important aspect is being investigated. A practical measure to quantify the efficiency of the acid treatment is the Skin reduction. The Skin causes an additional pressure drop (i.e. Δp_{skin}) near the wellbore region. The difference between the initial and final pressure drop is analysed; and being related to the acid treatment. For sensitivity purposes, the difference in Δp_{skin} is plotted in Figure 6.2 as a function of the acid dissolving power. For which the 1D FIM model is used with the injection rate and reservoir pressure as the left and right boundary condition, respectively. The corresponding input data is presented in Table 5.1.

An example, for an acid dissolving power of $200 g/mol$, is displayed in Figure 6.1. The initial pressure at the left boundary is approximately $270 bar$. After completion of the acidizing treatment the pressure dropped to approximately $200 bar$. Consequently, the difference in Δp_{skin} is approximately $70 bar$.

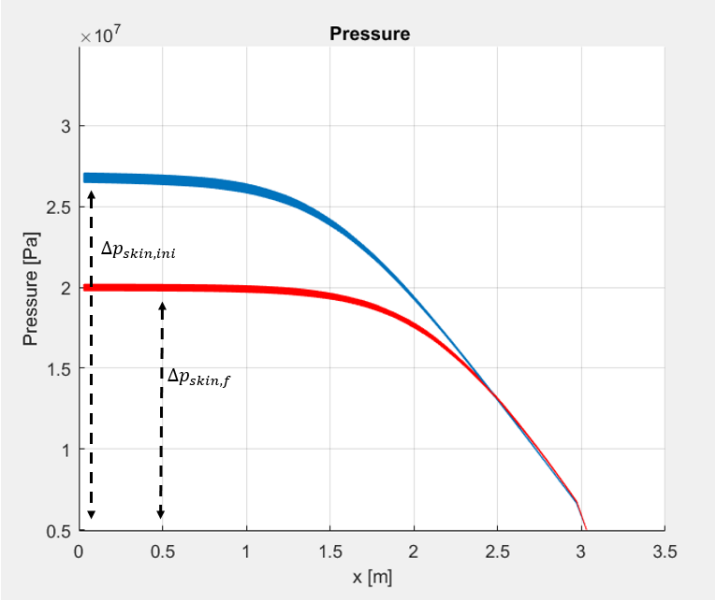

Figure 6.1: Pressure drop due to reaction kinetics. The acid dissolving is set to $200 g/mol$. Additional input data is stored in Table 5.1

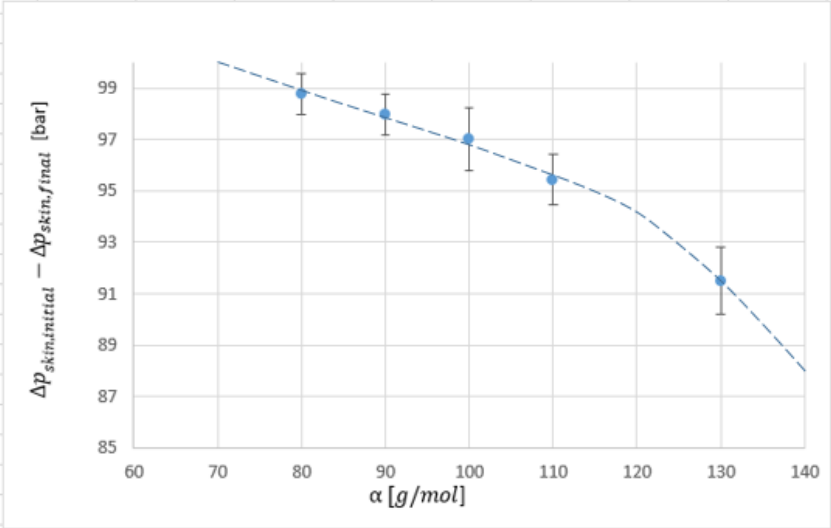

Figure 6.2: Sensitivity study of the $\Delta p_{skin,Initial}$-$\Delta p_{skin,final}$ after 2 hours of injection as a function of the acid dissolving power. Additional input data can be found in Table 5.1

CHAPTER 7

CONCLUSION AND FUTURE WORK

Two approaches were developed to simulate carbonate matrix acidizing at the “larger scale”. The initial approach comprises of a sequential strategy. For stability reasons, a second model was developed. This fully implicit model (i.e. FIM) allowed for a more stable and robust treatment of the coupling between the reaction kinetics and fluid dynamics. As such, it formed the core of the delivered simulator to Akzonobel co.

The developed model is tailored for the reaction kinetics of the Dissolvine® Stimwell product. Based on the reaction kinetics of this product, the reaction rate was assumed to be instantaneous. The model incorporates both flow trough porous medium and free flow (i.e. flow trough wormholes). Achieved by implementation of the Darcy-Stokes relationship.

The simulation results were compared with experimental results at unprecedented [15] and core scales. These studies were performed to validate the trend of the wormhole configurations (and creations) depending on the injection flow rate.

At both scales, the trends were in good agreement with the expected ones from the experiments. This provides a valuable confirmation that a simplified Brinkman-based simulator with the upscaled reaction properties can capture the dependencies at near wellbore region. This study has never been done in the community, and casts the core of the novelty of this thesis work.

Finally, as for the important operational knowledge about the efficiency of the acid treatment, the improvement in the productivity of the well –measured in terms of reduction of Skin factor– was also studied briefly in this work.

It is important to emphasize that many interesting challenges remain for future work:

- It is interesting to develop a simulator on a cylindrical coordinate system, to include the

radial behavior of the flow pattern around the well.

- In addition, consideration of multiphase flow around the well (with capillary pressure consideration) seems quite important as the existence of other phases may influence the penetration of the acid in the reservoir.
- Additional studies concerning the empirical dependency of the permeability to the porosity and the interfacial area per unit volume are necessary, specially for domains with a combination of free flow (i.e. wormholes) and porous medium.
- The possibilities of enhancing the computational efficiency of the FIM model by integrating it with the Algebraic Dynamic Multiscale (i.e. ADM) [5, 26] method using monotone multiscale formulation [27] allows for an increase of computational efficiency while maintaining the fine scale accuracy.

NOMENCLATURE

Quantity	Unit	Meaning
α	g/mol	dissolving power of acid
a_v	m^{-1}	Interfacial area per unit volume of medium
u	m/s	Horizontal velocity
K	m^2	Permeability
K_0	m^2	Initial permeability
C_f	mol/L	Concentration of acid in the fluid phase
p	Pa	Pressure
Q	m^3/s	Flow rate
μ	Pa.s	Fluid viscosity
p_{skin}	Pa	Additional pressure drop caused by formation damage
S	-	Skin factor
PV	m^3	Pore volume
PVBT	-	Pore volume to breakthrough ($PV_{final}/PV_{initial}$)
ϕ -	Porosity	
V	m^3	Volume
A	m^2	Area
k_c	m/s	Local mass transfer coefficient
β	-	pore structure relation constant
p_R	Pa	Pressure at the right boundary
L_x	m	Length in the x direction
L_y	m	Length in the y direction
ρ_s	kg/m^3	density of the carbonate rock
Nx	-	Grid cells in the x direction
Ny	-	Grid cells in the y direction
De	m^2/s	Effective dispersion tensor

BIBLIOGRAPHY

[1] O. O. AKANNI AND H. A. NASR-EL-DIN, *Modelling of wormhole propagation during matrix acidizing of carbonate reservoirs by organic acids and chelating agents*, Society of Petroleum Engineers, (2016).

[2] AKZONOBEL, *Dissolvine gl technical brochure*, AkzoNobel Chelates and Micronutrients, (2016).

[3] R. C. BREWER, J. C. BOLTON, AND S. G. DRIESE, *A new classification of sandstone*, Journal of Geological education, (1990).

[4] I. M. CHESHIRE, J. R. APPLEYARD, D. BANKS, R. J. CROZIER, AND J. A. HOLMES, *An efficient fully implicit simulator*, SPE, (1980).

[5] M. CUSINI, C. VAN KRUIJSDIJK, AND H. HAJIBEYGI, *Algebraic dynamic multilevel (adm) method for fully implicit simulations of multiphase flow in porous media*, Journal of Computational Physics, 314 (2016), pp. 60–79.

[6] C. N. FREDD AND H. SCOTT FOGLER, *The influence of chelating agents on the kinetics of calcite dissolution*, Journal of colloid and interface science, (1998).

[7] M. T. HALBOUTY, A. A. MEYERHOFF, R. E. KING, R. H. DOTT, S. H. D. KLEMME, AND T. SHABAD, *World's giant oil and gas fields, geologic factors affecting their formation, and basin classigication*, AAPG, (1970).

[8] H. LABAUZE, *Scale mechanisms and chemical mitigation options in wells, reservoirs and treatment facilities*, Nederlandse Aardolie Maatschappij, (2014).

[9] X. LIU, A. ORMOND, K. BARTKO, AND P. O. YING LI, *A geochemical reaction-transport simulator for matrix acidizing analysis and design*, Journal of Petroleum Science and Engineering, (1996), pp. 182–195.

[10] P. L.N, W. T.M.L, P. D.L, AND A. J. SCI., *Critical review of the kinetics of calcite dissolution and precipitation*, U.S. Geological Survey, Reston, VA 22092, (1978).

[11] F. J. LUCIA, *Carbonate reservoir characterization: An integrated approach*, Book published by Springer, (1990).

[12] K. LUND, H. FOGLER, AND C. M. CUNE, *The dissolution of dolomite in hydrochloric acid*, Chevron Oil Field Research company, (1972).

[13] M. MAHMOUD, H. NASR-EL-DIN, C. D. WOLF, AND J. LEPAGE, *Stimulation of carbonate reservoirs using glda (chelating agent) solutions*, SPE, (2010).

[14] M. MAHMOUD, H. NASR-EL-DIN, C. D. WOLF, J. LEPAGE, AND J. BEMELAAR, *Evaluation of a new environmentally friendly chelating agent for high-temperature applications*, SPE, (2011).

[15] D. R. MCDUFF, C. E. SCHUCHART, S. K. JACKSON, D. POSTL, J. S. BROWN, AND E. UPSTREAM RESEARCH COMPANY, *Understanding wormholes in carbonates: Unprecedented experimental scale and 3-d visualization*, SPE, (2010).

[16] N. MUMALLAH, *Factors influencing the reaction rate of hydrochloric acid and carbonate rock*, Society of Petroleum Engineers, (1991).

[17] M. K. R. P. NAD MURTAZA ZIAUDDIN, *Two-scale continuum model for simulation of wormholes in carbonate acidization*, Dept. of Chemical Engineering, University of Houston, Houston, TX 77204, (2005).

[18] G. NAELE AND W. NADER, *Practical significance of brinkman's extension of darcy's law: Coupled parallel flows within a channel and a bounding porous medium*, The Canadian Journal of Chemical Engineering, (1974).

[19] E. A. NOOR AND A. H. AL-MOUBARAKI, *Corrosion behavior of mild steel in hydrochloric acid solutions*, International Journal of Electrochemical science, (2008).

[20] O. O., AKANNI, H. A., AND NASR-EL-DIN, *Modeling of wormhole propagation during matrix acidizing carbonate reservoirs by organic acids and chelating agents*, Society of Petroleum Engineers, (2016).

[21] P.MAHESHWARI AND V. BALAKOTAIAH, *Comparison of carbonate hcl acidizing experiments with 3d simulations*, SPE Production and operations, (2013).

[22] S. PORTIER AND L. A. . F.-D. VUATEZ, *Review on chemical stimulation techniques in oil industry and applications to geothermal systems.*, Centre de recherche en geothermie, (2007).

[23] H. SCOTT FOGLER AND C. N. FREDD, *Influence of transport and reaction on wormhole formation in porous media*, Dept. of Chemical Engineering, University of Michigan, Ann Arbor, MI 48109, (1998).

[24] R. E. SERVIES, *Under balanced drilling (ubd)*, https://www.reformenergy.com/ubd.

[25] R. SHIRLEY, D.ZHU, A. HILL, AND E. D. MOTTA, *Maximizing the value of matrix acidizing treatments in carbonate reservoirs*, SPE, (2017).

[26] M. TENE, Y. WANG, AND H. HAJIBEYGI, *Adaptive algebraic multiscale solver for compressible flow in heterogeneous porous media*, J. Comp. Phys., 300 (2015), pp. 679–694.

[27] Y. WANG, H. HAJIBEYGI, AND H. TCHELEPI, *Monotone multiscale finite volume method*, Computational Geosciences, 20 (2015), pp. 509–524.

[28] U. O. O. XINGHUI LIU, FARUK CIVAN, *Formation damage and skin factor due to filter cake formation and fines migration in the near wellbore region*, SPE, (2017), pp. 250–273.

[29] A. ZEINIJAHROMI, A. VAZ, AND P. BEDRIKOVETSKY, *Well impairment by fines migration in gas fields*, Journal of Petroleum Science and Engineering, (2012).